CrossMark

INVITED ARTICLE

# Continuum modeling of $B_4C$ densification during Spark Plasma Sintering

Ji-an Liu, Fanhao Zeng,[a] Zhihuan Zou, and Yi Li
*Science and Technology on High-Strength Structural Materials Laboratory, Central South University, Changsha 410083, China*

Yi Gu
*School of Materials Science and Engineering, Central South University, Changsha 410083, China*

Fuqin Zhang
*Science and Technology on High-Strength Structural Materials Laboratory, Central South University, Changsha 410083, China*

Tongxiang Liang
*State Key Laboratory of New Ceramic and Fine Processing, Tsinghua University, Beijing 100084, China*

(Received 13 January 2017; accepted 8 May 2017)

Boron carbide ($B_4C$) powder was consolidated at 45 MPa by Spark Plasma Sintering (SPS) for 20 min from 1450 to 2000 °C. The density of the $B_4C$ reached 99.6% at 2000 °C. A continuum model was applied to describe the densification mechanism of $B_4C$ powder under SPS conditions. The shrinkage rate was sensitive to particle size and temperature. The effect of porosity on thermal diffusion was significant, especially for small particle sizes. It appears that there is Joule heating, discharge, and electromagnetic field involved during the SPS of $B_4C$. The current can enhance the sintering process, and it can obviously reduce the creep activation energy.

## I. INTRODUCTION

Boron carbide ($B_4C$) is an attractive covalently bonded ceramic with low density (2.52 g/cm$^3$), high melting point (2450 °C), high Young's modulus (>435 GPa), and especially high Vickers hardness (>27 GPa). Furthermore, $B_4C$ has good chemical inertness, low thermal expansion coefficient ($5.7 \times 10^{-6}$/°C), and high neutron absorption cross-section. Due to these outstanding properties, $B_4C$ ceramic has great potential for many applications such as neutron absorber, blasting nozzles, wear-resistant components, and especially light armor.[1–7] However, it's difficult to obtain high density pure $B_4C$ by pressureless sintering methods due to the high of covalency of bonds between B and C atoms in $B_4C$ (>90%).[8] Thus high temperatures close to the melting point of $B_4C$ are required to achieve complete densification, which results in grain coarsening and degenerated material' properties. Hot-pressing (HP) can lower the consolidation temperature of $B_4C$ ceramics but the relative density only reaches 92–98% when the pressure and temperature are 30–40 MPa and 2000–2100 °C respectively.[7] Sintering aid additions like pure metal (Al, Ti, Fe, Ni, Cu, Cr), metal oxides and metal salts (MgO, $Fe_2O_3$, $Al_2O_3$, $TiO_2$, $Na_2SO_4$), metal carbide and boride (TiC, $TiB_2$, SiC, CrC, CrB) are reported to lower the sintering temperature of $B_4C$ ceramics.[9–13] However, owing to the complex composition and reaction between carbide and sintering aids, the purity of final produce limits its application in nuclear industries.

Spark Plasma Sintering (SPS), also known as electric-discharge sintering or field-assisted sintering, is a fast sintering technology that combines the application of pressure and current directly or indirectly to consolidate the powder. It was suggested that due to the presence of a plasma between powder particles, the powder surface can be activated and thus the powder sintered to outstanding properties and limited grain growth at low temperature and short heating time.[14,15] Recently, researchers have reported the microstructure, properties, and densification behavior of $B_4C$ prepared by SPS at different sintering atmosphere, pressure, and temperature.[16–19] Xu[20] obtained a relative density of 99.1% boron carbide samples by SPS at 1700–1750 °C for holding time of 5 min with sintering aids $CaF_2$/$Y_2O_3$. Sairam[21] reported the influence of sintering parameters on the physical properties of boron carbide. It was found that near full density $B_4C$ samples can be obtained by SPS at 1800 °C, 50 MPa and heating time of 15 min.

It is well known that SPS involves both heating and field effects, and thus the forming mechanism of SPS is very complex. Trial and error are mostly used to get an experimental densification law.[18,22] Bernard–Granger[23] proposed a densification mechanism of $ZrO_2$ powder during the SPS experiments. When the stress/temperature is low, it is indicated that only diffusion mechanism controlled

Contributing Editor: Gary L. Messing
[a]Address all correspondence to this author.
e-mail: zengfanhao608@csu.edu.cn
DOI: 10.1557/jmr.2017.205

 © Materials Research Society 2017 

https://doi.org/10.1557/jmr.2017.205 Published online by Cambridge University Press

the densification. At a stress exponent of 2, the densification proceeds by grain boundary sliding accommodated by interface-reaction. For high stress, the densification of $ZrO_2$ powder was determined by a dislocation-climb-controlled mechanism. Recently, Olevsky[22,24,25] developed an SPS densification mechanism model based on concepts of continuum theory of sintering. The continuum model is on the basis of the traditional hot pressing model and takes into account the current effect. Two kinds of powder, Al and $Al_2O_3$, were sintered by SPS and their theoretical densification curves were calculated by the continuum model. The theoretical curves agreed well with the experimental results. However, considering a large number of influencing factors, especially for the high melting point of carbide ceramic powder in SPS, the theoretical calculation result needs more experimental verification for various materials. In this work, $B_4C$ ceramic powder was consolidated using SPS at 1450–2000 °C. The density and microstructure were studied by optical microscopy (OM, Lecia MeF3A optical microscope, Leica Microsystem GmbH, Wetzlar, Germany), scanning electron microscopy (SEM, Philips XL30 ESM, Amsterdam, the Netherlands), and X-ray diffraction (XRD; Rigaku 3014 X-ray diffractometer, Tokyo, Japan). To obtain the densification kinetics of $B_4C$ compacted by SPS, the constitutive model based on the continuum theory of sintering was applied for the first time. The effect of temperature, pressure, current, and heating rate on the densification of $B_4C$ is discussed in detail.

## II. EXPERIMENTAL

$B_4C$ powder (Mudanjiang Boron Carbide Co. Ltd, China, $D_{50}$ = 3.5 μm) and boron nitride (BN) powder (Yingkou Liaobin Fine Chemical Co. Ltd, China) were used as starting powder. The powders that keep the mass ratio of $B_4C$:BN = 100:1 were mixed and balled in ethanol for 3 h using WC-Co cemented carbide balls. After drying at 100 °C for 12 h, the mixed powder was filled into a cylindrical graphite die with inside diameter of 40 mm. Two piece of 0.45 mm thick graphite sheet were placed on the top and bottom of the sample to prevent adhesion and contamination between the specimen and the graphite die. The die with powders was then carefully loaded into a SPS apparatus (D25/3, FCT System, Rauenstein, Germany) equipped with 57 kN uniaxial press. The densification was performed in the temperature range of 1450–2000 °C with dwell time of 20 min. Generally, the heating rate was maintained at 100 °C/min. An Argon atmosphere was utilized in all SPS experiment to prevent the furnace chamber and the heating elements from being overheated. After sintering, the disc shaped samples were ground with abrasive SiC paper to remove the adherent graphite foil from the outer surfaces.

The density of sintered samples was measured by Archimedes' method with deionized water. After density measurement, specimens were cut by wire-electrode cutting machine and subsequently ground with diamond disc, then polished with a colloidal diamond suspension. The well polished surfaces were etched using a modified Murakami's solution (15 g $K_3FeCN_6$ and 15 g KOH in 60 mL of water) at 100 °C for about 30 min. Polished and etched samples were observed using optical (OM; Lecia MeF3A) and scanning electron microscopy (SEM; Philips XL30) with an energy dispersive X-ray spectrometer attachment (INCA, Oxford), respectively. The grain size was determined from the SEM and optical micrographs and the average particle diameter was determined by the equivalent circle method. The crystal structure and lattice parameters were evaluated by X-ray diffraction (XRD; Rigaku 3014) utilizing Cu $K_\alpha$ radiation at room temperature.

## III. RESULTS AND DISCUSSION

### A. Density and microstructure

The densities, microstructure, and XRD patterns of $B_4C$ samples sintered by SPS at temperatures varying from 1450 to 2000 °C are shown in Fig. 1. Figure 1(a) plots the densities of $B_4C$ samples as a function of the processing temperature. It appears that with the sintering temperature increasing, the density of boron carbide increases. The density of $B_4C$ achieves near theoretical density of 2.51 g/cm$^3$ at 2000 °C. Three different sintering stages were observed within the temperature range of 1450–2000 °C. In the first stage of sintering, densification of $B_4C$ is found to be slow when the temperature is <1600 °C. During the second stage of sintering, the density increases suddenly and it has steeper slope when the sintering temperature is 1600–1900 °C, which indicates that the $B_4C$ powder has rapid densification during the temperature range and it plays a dominant role in the densification of $B_4C$. During the third stage or final stage of densification, the density curve of $B_4C$ have slowest rate due to the elimination of residual porosities. Because of the different powder sizes of initial $B_4C$ powder, the increase densification rate has some differences from the reported literature data.[21]

Figure 1(b) shows the typical optical microstructures of etched $B_4C$ specimens sintered at 2000 °C. The grains are equiaxed and 2–10 μm in size. The average size of $B_4C$ grains is 3.1 μm, which is close to the mean particle size (3.5 μm) of the initial powder. It is worthwhile pointing out that the grain shape and sizes of as-produced $B_4C$ are different from hot-pressing $B_4C$ samples, which appear to have straight grain boundaries and a wide range of particle sizes of 6–48 μm.[26] These results indicates that due to the short sintering time of SPS, the $B_4C$ grains are not grown even at their full densification temperature, which reflects the advantage of SPS method.

XRD patterns of boron carbide samples sintered by SPS at 1450, 1700, 2000 °C are shown in Fig. 1(c). No additional oxidation phase was observed during sintering process. The peaks for $B_4C$ can be clearly observed in the patterns and

https://doi.org/10.1557/jmr.2017.205 Published online by Cambridge University Press

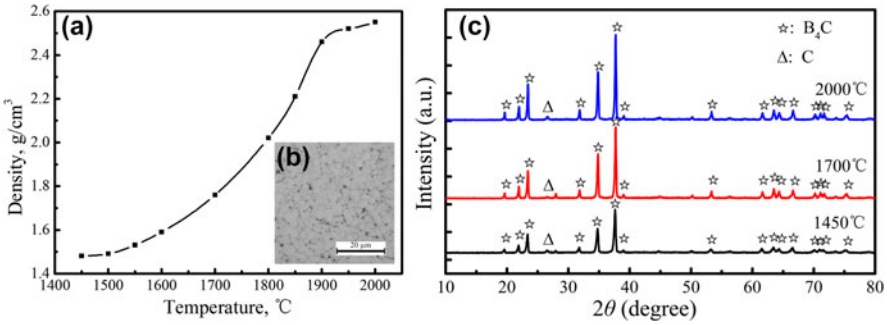



FIG. 1. (a) Density of SPS $B_4C$ samples sintered as a function of sintering temperature for 20 min; (b) the optical microstructures of 99.6% dense $B_4C$ compact sintered at 2000 °C for 20 min, (c) the XRD patterns of $B_4C$ at 1450, 1700 and 2000 °C for 20 min prepared by SPS.

the main peak positions do not move with different sintering temperature, which indicates that $B_4C$ is very stable in the SPS sintering process. A small peak in the XRD pattern is observed at about $2\theta = 26.51°$, which was assigned to graphite.[18] There are two sources of graphite in the samples. The main source is from the raw powders of $B_4C$ and other maybe diffused from the graphite foil during the sintering.

SEM micrographs of $B_4C$ prepared at 1450, 1600, 1850, 2000 °C for 20 min are shown in Fig. 2. It is clearly observed that increasing sintering temperature, the porosity decreased and the density of $B_4C$ was increased significantly. Grain growth was not observed at 1450 °C as shown in Fig. 2(a). At 1700 °C [Fig. 2(b)], sintering necks appeared and the samples still had interconnected porosity. When the sintering temperature was ≥1850 °C [Fig. 2(c)], there was isolated individual small pores displayed in the matrix and the relative density reached 87.7%. Nearly fully dense sample (relative density 99.6%) was obtained after sintering at 2000 °C [Fig. 2(d)]. In addition, some low-density crystal defects, such as twins, were observed in the sample [Fig. 2(d)]. It is well known that boron carbide has a α-rhombohedral crystal structure, which is hard to slip in plastic deformation. During applied pressure and high temperature; however, it can deformed by mechanical twinning or growth twinning mode, which need higher deformation stored energy and may shear to the matrix. The nucleation and growth mechanisms of these compression twins in boron carbide is need for further investigation.

## B. Model and calculation

### 1. The Olevsky continuum model

The Olevsky continuum model is based on the traditional hot-pressing model and accounts for electric. The model framework includes three constitutive models which consider external load, surface tension, and a temperature gradient.[22]

#### a. Power-law creep mechanism of material transport

Considering the SPS pressing in a rigid die, the deformation of material occurs only in the $x$ direction (the piston displacement direction). The equation was derived by Olevsky can be represented as:

$$\dot{\varepsilon}_{crx} = -\left\{ \frac{\left(\frac{3\theta}{2}\right)^{\frac{m+1}{2}} \left[\frac{3\alpha}{2G}(1-\theta)^2 - \bar{\sigma}_x\right]}{A(1-\theta)^{\frac{m+3}{2}}} \right\}^{\frac{1}{m}}, \quad (1)$$

where $\dot{\varepsilon}_{crx}$ is the macroscopic shrinkage rate, $\bar{\sigma}_x$ is effective (far-field) external stress in the $x$ direction; $\alpha$ is the surface tension; $A$ and $m$ are the power-law creep frequency factor and the power-law creep exponent, respectively; $G$ is the average particle radius, $\theta$ is the porosity.

Following Olevsky,[25] the power-law frequency factor can be written as:

$$A = A_0 \exp\left(-\frac{Q_{cr}}{RT}\right), \quad (2)$$

where $A_0$ is the power-law creep frequency factor, $Q_{cr}$ is the creep activation energy; $T$ is the absolute temperature, and $R$ is the gas constant.

This equation mainly describes the macroscopic phenomena. For a specific material, the shrinkage rate due to the power-law mechanism was only influenced by $G$, $T$, $\bar{\sigma}_x$, and $\theta$.

#### b. Grain-boundary diffusion driven by an externally applied load and surface tension

Grain-boundary diffusion is another major mechanism of mass flux for SPS. Figure 3 shows the micro-mechanic model for a powder compact of simple-packed, rectangular grains with semi-axes $a$ and $c$ and elliptical pores located at the grain Quadra-junctions. This constitutive modeling was developed from early micro–mechanic model of the grain-boundary diffusion under applied pressure, and from the model of power-law creep under hot deformation of powders. The macroscopic shrinkage rate $\dot{\bar{\varepsilon}}^{st}_{gbx}$ of the grain-boundary diffusion mechanism can be represented as:

https://doi.org/10.1557/jmr.2017.205 Published online by Cambridge University Press

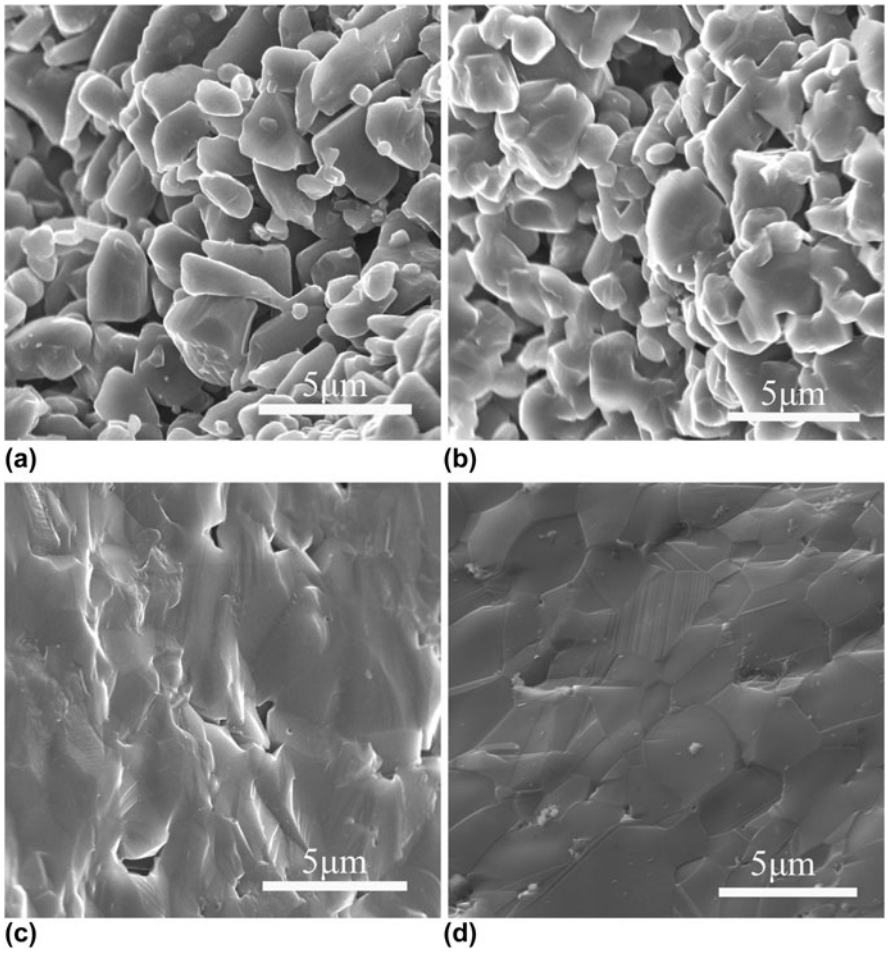



FIG. 2. SEM images of the $B_4C$ samples sintered at (a) 1450 °C, (b) 1600 °C, (c) 1850 °C, and (d) 2000 °C under the heating rate of 100 °C/min and the holding time of 20 min.

$$\dot{\bar{\varepsilon}}^{st}_{gbx} = -\frac{9\alpha\delta_{gb}D_{gb}\Omega}{4\pi kTG^4}\frac{\left(\sqrt{\pi}-2\sqrt{\theta}\right)^2}{1-\theta} \times\left\{\left(\sqrt{\pi}-3\sqrt{\theta}\right)\sqrt{\theta}-\frac{2\sqrt{\pi}\theta}{9(1-\theta)^2\left(\sqrt{\pi}-2\sqrt{\theta}\right)}\left(\frac{\bar{\sigma}_x G}{\alpha}\right)\right\}, \quad (3)$$

where, $D_{gb}$ and $\delta_{gb}$ are the diffusion coefficient and the thickness of the grain-boundary, respectively; $k$ is the Boltzmann constant; $\Omega$ is the atomic volume.

For a specific material, the shrinkage rate was only influenced by $G$, $T$, $\bar{\sigma}_x$, and $\theta$. This modeling only considered the effect of grain-boundary diffusion on the shrinkage rate or the density.

### c. Thermal diffusion contributing to the intensification of densification during SPS

Based on the flux (along various paths) equation corresponding to thermal diffusion, the macroscopic

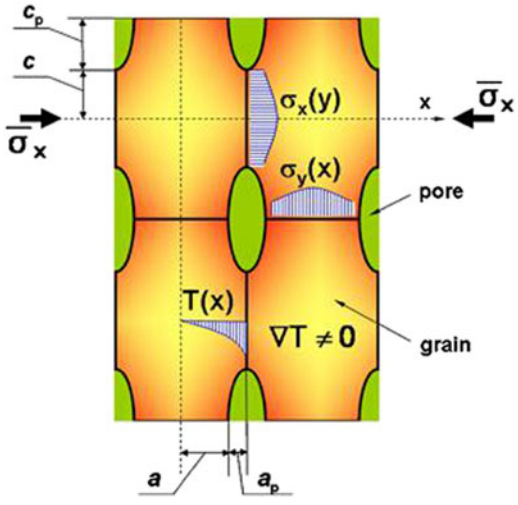



FIG. 3. Pore-grain structure unit cell. Rectangular grains with semi-axes $a$ and $c$ contain elliptical pores with semi-axis $a_p$ and $c_p$ located at the grains' Quadra-junctions. Temperature and stress gradients are nonzero along grain boundaries.[22]

https://doi.org/10.1557/jmr.2017.205 Published online by Cambridge University Press

contribution of thermal diffusion to the shrinkage rate $\bar{\dot{\varepsilon}}^{td}_{gbx}$ was derived:

$$\bar{\dot{\varepsilon}}^{td}_{gbx} = -\frac{\delta_{gb} D_{gb} \Omega C_V H_m}{\lambda_T k \langle T \rangle^2} \left( C \frac{\partial T}{\partial t} - \lambda_e E^2 \right) \times \frac{3\left(\sqrt{\pi} - 2\sqrt{\theta}\right)^2 \theta}{2\pi G (1-\theta)} \quad , \tag{4}$$

where, $\langle T \rangle$ is the spatial average of temperature; $H_m$ is the enthalpy of vacancy migration; $C_V$ is the vacancy concentration; $\lambda_T$ is the thermal conductivity; $C$ is the heat capacity; $t$ is the time; $\lambda_e$ is the specific electric conductivity; $E$ is the electric field intensity.

In SPS method, the heating rate is more higher than hot-pressing methods. According to this model, when $\left| C \frac{\partial T}{\partial t} - \lambda_e E^2 \right| \gg 0$, the thermal diffusion has a great influence on SPS. Only the terms $\lambda_e E^2$ and $C \frac{\partial T}{\partial t}$ have the same order of magnitude, the heating rate $\frac{\partial T}{\partial t}$ can be significantly influenced by the shrinkage rate $\bar{\dot{\varepsilon}}^{td}_{gbx}$.

The combined contributions of the grain-boundary diffusion [Eq. (3)], power-law creep [Eq. (1)], and thermal diffusion [Eq. (4)] to the shrinkage rate under SPS are given by:

$$\dot{\varepsilon}_x = \bar{\dot{\varepsilon}}^{st}_{gbx} + \dot{\varepsilon}_{crx} + \bar{\dot{\varepsilon}}^{td}_{gbx} \quad . \tag{5}$$

For the calculation of the porosity (relative density), the following continuity (mass conservation) equation is used:

$$\frac{\dot{\theta}}{1-\theta} = \dot{\varepsilon}_x \quad . \tag{6}$$

Substituting Eqs. (1)–(4) and (6) in Eq. (5), we obtain the Olevsky continuum model of SPS [Eq. (7)]:

$$\begin{aligned} \frac{\dot{\theta}}{1-\theta} = \dot{\varepsilon}_x = & -\frac{9\alpha \delta_{gb} D_{gb} \Omega}{4\pi k T G^4} \frac{\left(\sqrt{\pi} - 2\sqrt{\theta}\right)^2}{1-\theta} \\ & \times \left\{ \left(\sqrt{\pi} - 3\sqrt{\theta}\right)\sqrt{\theta} - \frac{2\sqrt{\pi}\theta}{9(1-\theta)^2\left(\sqrt{\pi} - 2\sqrt{\theta}\right)} \left(\frac{\bar{\sigma}_x G}{\alpha}\right) \right\} \\ & - \left\{ \frac{\left(\frac{3\theta}{2}\right)^{\frac{m+1}{2}} \left[ \frac{3\alpha}{2G} (1-\theta)^2 - \bar{\sigma}_x \right]}{A_0 \exp\left(\frac{Q_{cr}}{RT}\right) (1-\theta)^{\frac{m+3}{2}}} \right\}^{\frac{1}{m}} \\ & - \frac{\delta_{gb} D_{gb} \Omega C_v H_m}{\lambda_T k \langle T \rangle^2} \left( C \frac{\partial T}{\partial t} - \lambda_e E^2 \right) \times \frac{3\left(\sqrt{\pi} - 2\sqrt{\theta}\right)^2 \theta}{2\pi G (1-\theta)} \quad . \end{aligned} \tag{7}$$

## 2. Calculation of the SPS densification $B_4C$ by the Olevsky continuum model

In the calculations, three parameters of $C$, $\lambda_T$ and $\lambda_e$ are functions of porosity $\theta$[22,27–30]:

$$\begin{aligned} C &= C_{fd}(1-\theta) \quad , \\ \lambda_T &= \lambda_{Tfd}\left(1 - \frac{3}{2}\theta - \frac{1}{2}\theta^2\right) \quad , \\ \lambda_e &= \lambda_{efd} \frac{1-\theta}{1+2\theta} \quad , \end{aligned} \tag{8}$$

where, $C_{fd}$, $\lambda_{Tfd}$, and $\lambda_{efd}$ are the heat capacity, the heat conductivity and the electric conductivity of the fully dense material.

The contributions of different mass transport mechanisms ($\bar{\dot{\varepsilon}}^{st}_{gbx}$, $\dot{\varepsilon}_{crx}$, $\bar{\dot{\varepsilon}}^{td}_{gbx}$) to the overall shrinkage rate of $B_4C$ under SPS conditions are calculated based on Eq. (7) and shown in Fig. 4. It shows that thermal diffusion contribution to the shrinkage rate is significant, especially for high temperatures and smaller particle sizes. For a boron carbide powder, the electric field is assumed to be 300 V/m, porosity $\theta$ is 0.3, the externally applied stress $\bar{\sigma}_x$ is 45 MPa, and the heating rate is 100 K/min. Two average particle sizes: $G$ = 3.5 μm [Fig. 4(a)] and $G$ = 7 μm [Fig. 4(b)] were analyzed. The material parameters for $B_4C$ are given in Table I.

During calculation, quantitative verification can be conducted by comparing the theoretically predicted densification kinetics with the experimental data. The temperature and pressure regimes used in the calculations replicate the conditions of the experiment. The pressure is expected to be constant and equal to 45 MPa. The boron carbide specimens with an initial porosity of 42% are assumed to be heated to 2000 °C at a rate of 100 °C/min. According to the previous SEM experimental results, we assumed that the particles did not grow during the SPS.

The shrinkage kinetics as well as the temperature is shown in Fig. 5. The modeling results for $B_4C$ are obtained by the numerical solution of the ordinary differential Eqs. (7) and (8) by the Runge–Kutta method of the 4th order. The experimental data for the shrinkage kinetics is also shown in Fig. 5. The results show that with increasing sintering time, the relative density of $B_4C$ decreases, and it is close to full density after 1000 s. The calculated results are agreement with the experimental points, except for a minor deviation in time at high temperature.

The influence of different sintering parameters on sintering behavior of $B_4C$ powder was calculated by continuum model. Figure 6(a) shows the shrinkage kinetics of $B_4C$ powder with different average particle sizes. It showed that the full-density temperature was decreased from 2000 to 1900 °C with a decrease of the initial particle size from 4 to 3 μm. Figure 6(b) shows the shrinkage kinetics of $B_4C$ powder with different heating rate. As the heating rate increased from 50 to 300 °C/min, the heating time required to achieve full density decreased from 1200 to 300 s. Figure 6(c) shows the shrinkage kinetics of $B_4C$ powder with different applied

https://doi.org/10.1557/jmr.2017.205 Published online by Cambridge University Press

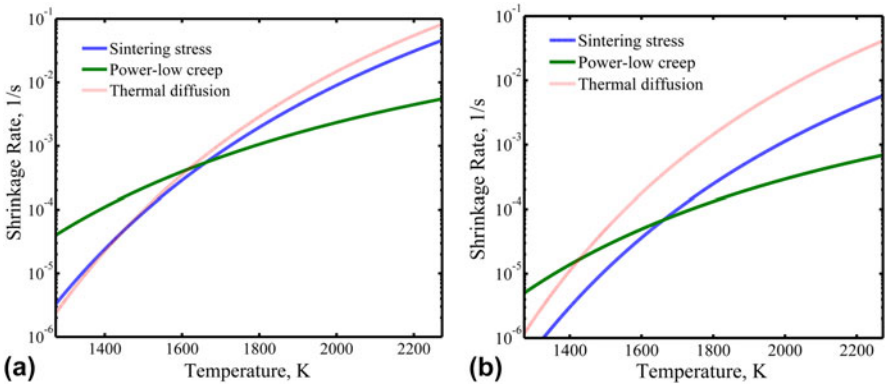



FIG. 4. Contribution to shrinkage rate from different mechanisms of mass transport by different grain size of $B_4C$ powder; (a) particle size $G$ = 3.5 μm; (b) particle size $G$ = 7 μm (electric field 300 V/m, applied stress 45 MPa, porosity 0.3, heating rate 100 K/min).

TABLE I. Material parameters for boron carbide.

| | | |
|---|---|---|
| Atomic volume | $\Omega$ | $3.246 \times 10^{-28}$ $m^3$ (Ref. 31) |
| Molecular weight | $\hat{A}_{B_4C}$ | 0.0553 kg/mol (Ref. 31) |
| Theoretical density | $\rho_{B_4C}$ | 2520 kg/$m^3$ (Ref. 32) |
| Surface tension | $\alpha$ | 3.21 J/$m^2$ (Ref. 33) |
| Grain-boundary diffusion frequency factor | $[\delta_{gb}D_{gb}]_0$ | $9.12 \times 10^{-18}$ $m^3$ (Ref. 34) (SiC[a]) |
| Activation energy for grain-boundary diffusion | $Q_{gb}$ | 184 kJ/mol (Ref. 9) |
| Activation energy for power-law creep | $Q_{cr}$ | 1038.5 kJ/mol (Ref. 35) |
| Power-law creep frequency factor | $A_0$ | 1894.1 MPa $s^m$ (Ref. 35) |
| Power-law creep exponent | $m$ | 0.5 (Ref. 35) |
| Electric conductivity | $\lambda_{efd}$ | 33 s/m (Ref. 36) |
| Heat conductivity | $\lambda_{Tfd}$ | $0.4256–3.7657 \times 10\,T^{-4} + 1.3234 \times 10^{-7}\,T^2–7.3688 \times 10^{-12}\,T^3$ W/(m K) (Ref. 37) |
| Heat capacity | $C_{fd}$ | $22.99 + 5.40 \times 10^{-3}\,T–10.72 \times 10^5\,T^{-2}$ J/($m^3$ K) (Ref. 38) |
| Enthalpy of vacancy formation | $H_f$ | 60.67 kJ/mol (Ref. 39) (SiC[a]) |
| Enthalpy of vacancy migration | $H_m$ | 146.4 kJ/mol (Ref. 40) (SiC[a]) |

[a]Refer to the parameters of the similar materials of silicon carbide.

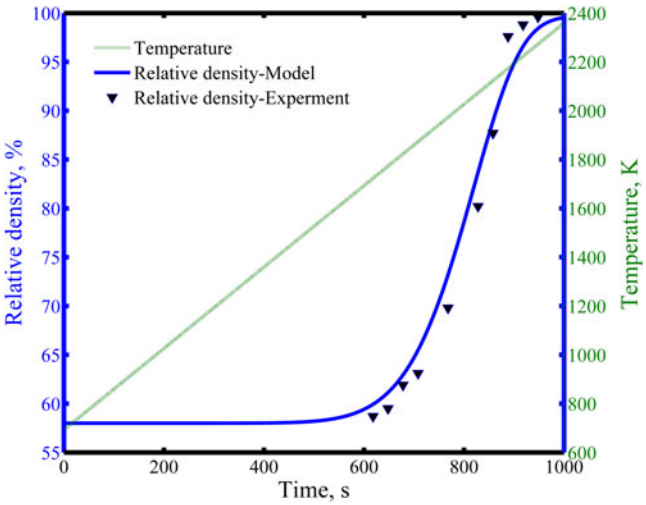



FIG. 5. Relative density kinetics of $B_4C$ powder versus sintering time during SPS. Comparison of the Olevsky continuum model (blue line) with experimental data (points).

stress. When the applied stress was increased, the sintering temperature decreased to achieve the same density. However, compared to the original particle size, the porosity is not so sensitive to applied stress in the range of 30–50 MPa during SPS.

## C. Role of the current

Joule heating from the large current (800–6500 A) passing through the die (typically graphite) and sample (if the sample is conducting) is the major difference between convention of hot-pressing and the SPS method. Passing of high current may have three roles: providing direct Joule heating, creating plasma, and changing in defect or enhancing mobility of the defects, which can enhance the sintering process.[14] The recent results reported by Olevsky[41] shows that the current passed through a copper specimen can achieve higher relative density than where no current was used at the same sintering condition. For the conducting sample, the current can pass through the sample and the die (if the die is conductive) directly, and then create a plasma between the contact point of two powder particles. This may lead to sintering enhancement, changing in defect, and enhancing mobility of the defects, and thus enhance mass transport. For the nonconducting sample, no current passed through the sample, and so the current only passes through the die. When the current crosses from the punch to the die (deflection current), a magnetic field was generated.[42] Variable magnetic field can generate an electric field, so an electromagnetic field was generated when the nonconducting sample was sintered by SPS.

https://doi.org/10.1557/jmr.2017.205 Published online by Cambridge University Press

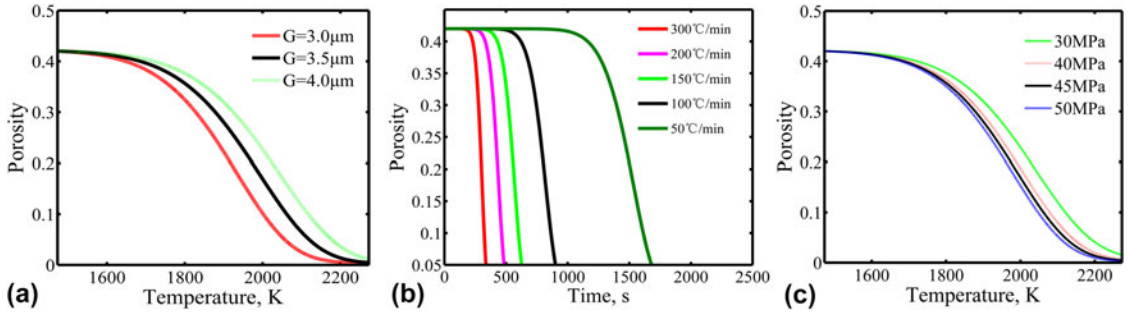



FIG. 6. Shrinkage kinetics of $B_4C$ powder with: (a) different average particle size (applied stress 45 MPa, heating rate 100 K/min), (b) different heating rate (applied stress 45 MPa, particle size 3.5 μm), (c) different applied stress (particle size = 3.5 μm, heating rate 100 K/min).

As a semiconductor, the electric conductivity of full density $B_4C$ was about 33 s/m. This may allow a part of current through the sample and another part of current passing though the die. Therefore, there may be Joule heating, discharge, and electromagnetic field during sintering process of $B_4C$. In initial stage, the contact points between the particles offer high resistance to the current flow, the temperatures at those localized heating zones would exceed the melting temperature of the powder and electric discharge may happen in this zones. Sairam et al.[19] reported the partial melted microstructure of $B_4C$ compact processed at 1800 °C by SPS, which is direct evidence for localized overheating mechanism. As the contacts between particles increase under pressure and heating, this phenomenon will becomes less and even disappear. The electromagnetic field only exists in heating-up period because there is no pulse current. During the late-stage of sintering, when the temperature has reached 2000 °C, it is found that thermal diffusion was the main diffusion mechanism (Fig. 4). At this stage, the effect of temperature on further densification was not obvious, where it mainly influence the grain shape and boundary. After holding for 20 min at 2000 °C, as shown in Fig. 2(d), the grain presented no-regular hexagonal shape and the partial melted structural may disappear. Particularly, because the current can enhance the sintering process, the creep activation energy used in the modeling was $\frac{5}{33}Q_{cr}$.

### D. Initial grain size and heating rate

As shown in Fig. 4, the effect of initial particle size on shrinkage rate is significant because particle size can change the mass transport mechanisms of $B_4C$ by SPS. For small particle size $B_4C$, thermal diffusion is the main mass transport mechanism. Figure 6(a) shows the shrinkage kinetics of $B_4C$ powder with different average particle size. The full density temperature was decreased from 2000 to 1900 °C with decrease of initial particle size from 4 to 3 μm.

Shrinkage kinetics of boron carbide powder with different heating rate is shown in Fig. 6(b). As the heating rate increased from 50 to 300 °C/min, the time required to achieve full density was decreased from 1200 to 300 s, indicating that the higher heating rate can effectively reduce the sintering time. Johnson[43] qualitatively confirmed that high heating rates can minimize the surface diffusion processes of alumina particles during SPS, but the heating rate has no obvious influence on the sintering temperature and density of alumina. In the present work, the calculated curve of porosity versus temperature was unchanged with the different heating rate, which agrees very well with result of alumina.

In the Olevsky continuum model, the constitutive equation of thermal diffusion contains the parameters of the heating rate $\frac{\partial T}{\partial t}$. From the part of the modeling $\left(C\frac{\partial T}{\partial t} - \lambda_e E^2\right)$, our calculation indicates that, even the heating rate range from 1 to 1000 °C/min, if assumed there is no particle coarsening during SPS, the shrinkage rate $\dot{\bar{\varepsilon}}^{td}_{gbx}$ only changes about 0.4‰. This change is relatively insignificant as compared with the total changes. Therefore, shrinkage kinetics of $B_4C$ powder sintered by SPS was insensitive to heating rate. But in some cases, particle/grain growth and heating rate are necessary to consider. Olevsky[25] derived the grain growth kinetics of aluminum:

$$\dot{G} = \begin{cases} \alpha\left(\frac{1}{K}\right)\varpi \ln\frac{235K/s}{\varpi} G_0\left(\frac{G_0}{G}\right)^3 \theta^{-1.34}, \text{ if } T > 533 \text{ K} \\ 0, \text{ if } T \le 533 \text{ K} \end{cases},$$

where, $\alpha$ is a constant, and $\varpi = dT/dt$ is the heating rate, K/s. From this expression, the grain growth kinetics was sensitive to particle size $G$ and heating rate $\varpi$. The modeling indicates that small particle size and higher heating rate can lower the sintering temperature effectively. Thus for some materials such as aluminum, shrinkage rate may be sensitive to heating rate.

### E. Applied stress

The constitutive modeling of power-law creep and sintering stress contain an important parameter of applied stress $\bar{\sigma}_x$. Figure 6(c) shows the calculated results of four



https://doi.org/10.1557/jmr.2017.205 Published online by Cambridge University Press

external applied stress: $\bar{\sigma}_x$ = 30 MPa, $\bar{\sigma}_x$ = 40 MPa, $\bar{\sigma}_x$ = 45 MPa and $\bar{\sigma}_x$ = 50 MPa. According to Eq. (1), it can be seen that the influence of stress on shrinkage rate $\dot{\varepsilon}_{crx}$ depends on the balance between the term $\frac{3\alpha}{2G}(1-\theta)^2$ and the term $\bar{\sigma}_x$. From our estimation, the value of $\bar{\sigma}_x$ is 2–10 times as large as the term $\frac{3\alpha}{2G}(1-\theta)^2$. Combining Eq. (3) with our estimates, it shows that the influence of stress on shrinkage rate $\bar{\dot{\varepsilon}}^{st}_{gbx}$ is minor. As shown in Fig. 6(c), with the applied stress increased, the sintering temperature was decreased. However, compared with other parameter such as the original powder particle size, the influence of external applied pressure on the density of boron carbide is very small and can be ignored in the 30–50 MPa range.

## IV. CONCLUSIONS

(1) Increasing the sintering temperature increases the density of boron carbide during SPS. The relative density of boron carbide exceeded 97% at 1900 °C and reached 99.6% at 2000 °C for 20 min.

(2) The theoretical densification process of $B_4C$ sintered by SPS was calculated based on the Olevsky continuum model, and it agrees well with the experimental results. It shows that the shrinkage rate of $B_4C$ by SPS is sensitive to particle size and temperature. The influence of external applied pressure on the density of boron carbide is very small during 30–50 MPa. The effect of thermal diffusion on shrinkage rate is significant, especially for small particle size.

(3) There may have Joule heating, discharge, and electromagnetic field in the process of sintering $B_4C$ by SPS. The current can enhance the sintering process, and it can obviously reduce the creep activation energy.

## ACKNOWLEDGMENTS

This work is supported by the National Natural Science Foundation of China (Grant No. 51301210), supported by State Key Laboratory of Powder Metallurgy of Central South University and State Key Laboratory of New Ceramic and Fine Processing of Tsinghua University.

## REFERENCES

1. F. Thevenot: A review on boron carbide. *Key Eng. Mater.* **56/57**, 59 (1991).
2. R.R. Ridgway: Boron carbide: A new crystalline abrasive and wear resisting product. *Trans. Am. Electrochem. Soc.* **66**, 117 (1934).
3. H.K. Clark and J.L. Hoard: The crystal structure of boron carbide. *J. Am. Chem. Soc.* **65**(11), 2115 (1943).
4. G.H. Tang, X.H. Zhang, and C.L. Chen: A comprehensive review on boron carbide. *Materials Review* **4**, 69 (1994).
5. F. Wu and J. Lu: Applications and the properties of boron carbide ceramic material. *Journal of Wuyi University* **16**, 45 (2002).
6. L.Z. Pei, H.N. Xiao, B.J. Zhu, and W. Tan: Latest development of boron carbide powder and diphase ceramics. *Rare Met. Cem. Carbides* **32**, 46 (2004).
7. K.W. Bai, Y.L. Wang, and J.F. Yang: The influence of hot pressing parameters on the microstructures and mechanical properties of boron carbide. *Journal of Xi'an Jiaotong University* **28**, 73 (1994).
8. B. Mu, H. Zhang, and L. Tang: Influence of the preparation technology on the properties of boron carbide. *Powder Metall. Technol.* **25**, 275 (2007).
9. R.G. Lange, Z.A. Munir, and J.B. Holt: Sintering kinetics of pure and doped boron carbide. *Mater. Sci. Res.* **13**, 311 (1980).
10. V. Skorokhod, M.D. Vlajic, and V.D. Krstic: Mechanical properties of pressureless sintered boron carbide containing $TiB_2$ phase. *J. Mater. Sci. Lett.* **15**, 1337 (1996).
11. L.S. Sigl: Processing and mechanical properties of boron carbide sintered with TiC. *J. Eur. Ceram. Soc.* **18**, 1521 (1998).
12. L.S. Wang: *Special Ceramic*, 2nd ed. (Central South Univ. press, Changsha, 2005); p. 186.
13. X.Y. Zhou: Low temperature sintering technology of boron carbide and its influencing factors. *Liaoning Chem. Ind.* **40**, 291 (2011).
14. Z.A. Munir, U. Anselmi-Tamburini, and M. Ohyanagi: The effect of electric field on the synthesis and consolidation of materials: A review of the spark plasma sintering method. *J. Mater. Sci.* **41**, 763 (2006).
15. R. Chaim: Densification mechanisms in spark plasma sintering of monocrystalline ceramics. *Mater. Sci. Eng., A* **443**, 25 (2007).
16. P. Badica, H. Borodianska, S. Xie, T. Zhao, and D. Demirskyi: Toughness control of boron carbide obtained by spark plasma sintering in nitrogen atmosphere. *Ceram. Int.* **40**, 3053 (2014).
17. S. Hayun, S. Kalabukhov, V. Ezersky, M.P. Dariel, and N. Frage: Microstructural characterization of spark plasma sintered boron carbide ceramics. *Ceram. Int.* **36**, 451 (2010).
18. X. Li, D. Jiang, J. Zhang, Q. Lin, Z. Chen, and Z. Huang: Densification behavior and related phenomena of spark plasma sintered boron carbide. *Ceram. Int.* **40**, 4359 (2014).
19. B.M. Moshtaghioun, D. Gómez-García, S.D. Bernardi-Martín, A. Domínguez-Rodríguez, and A. Monshi: Effect of spark plasma sintering parameters on microstructure and room-temperature hardness and toughness of fine-grained boron carbide ($B_4C$). *J. Eur. Ceram. Soc.* **33**, 361 (2013).
20. C. Xu, K. Flodström, and S. Esmaeilzadeh: Low temperature densification of $B_4C$ ceramics with $CaF_2/Y_2O_3$ additives. *Int. J. Refract. Met. Hard Mater.* **35**, 311 (2012).
21. K. Sairam, J.K. Sonber, T.S.R.C. Murthy, C. Subramanian, and R.K. Fotedar: Influence of spark plasma sintering parameters on densification and mechanical properties of boron carbide. *Int. J. Refract. Met. Hard Mater.* **42**, 185 (2014).
22. E.A. Olevsky: Impact of thermal diffusion on densification during SPS. *J. Am. Ceram. Soc.* **92**, S122 (2009).
23. G. Bernard-Grainger and C. Guizard: Spark plasma sintering of a commercially available granulated zirconia powder: I. Sintering path and hypotheses about the mechanism(s) controlling densification. *Acta Mater.* **55**, 3493 (2007).
24. E.A. Olevsky and L. Froyen: Constitutive modeling of sparking-plasma sintering of conductive materials. *Scr. Mater.* **55**, 1175 (2006).
25. E.A. Olevsky: Consolidation enhancement in spark-plasma sintering: Impact of high heating rates. *J. Appl. Phys.* **102**, 114913 (2007).
26. H.B. Wu, F.H. Zeng, and T.C. Yuan: Wettability of 2519Al on $B_4C$ at 1000–1250 °C and mechanical properties of infiltrated $B_4C$–2519Al composites. *Ceram. Int.* **40**, 2073 (2014).
27. E.A. Olevsky and A. Molinari: Instability of sintering of porous bodies. *Int. J. Plast.* **16**, 1 (2000).

https://doi.org/10.1557/jmr.2017.205 Published online by Cambridge University Press

28. E.A. Olevsky and A. Molinari: Kinetics and stability in compressive and tensile loading of porous bodies. *Mech. Mater.* **38**, 340 (2006).
29. R.L. Coble and W.D. Kingery: Effect of porosity on physical properties of sintered alumina. *J. Am. Ceram. Soc.* **39**, 377 (1956).
30. J.C. Maxwell: A treatise on electricity and magnetism. In *Thermal Conductivity of Solids*, J.E. Parrott and A.D. Stuckes, eds. (Pion Lid, London, 1975).
31. S.V. Konovalikhin and V.I. Ponomarev: Carbon in boron carbide: The crystal structure of $B_{11.4}C_{3.6}$. *Russ. J. Inorg. Chem.* **54**, 197 (2009).
32. V. Paris, N. Frage, M.P. Dariel, and E. Zaretsky: The spall strength of silicon carbide and boron carbide ceramics processed by spark plasma sintering. *Int. J. Impact. Eng.* **37**, 1092 (2010).
33. T.D. Beaudet, J.R. Smith, and J.W. Adams: Surface energy and relaxation in boron carbide $(10\bar{1}1)$ from first principles. *Solid State Commun.* **219**, 43 (2015).
34. E. Friedland, N.G.V.D. Berg, J.B. Malherbe, J.J. Hancke, and J. Barry: Diffusion of fission products through silicon carbide. In *International Topical Meeting on Nuclear Research Applications and Utilization of Accelerators* (International Atomic Energy Agency, Vienna, 2009); p. 8.
35. M.S. Koval'Chenko, Y.G. Tkachenko, L.F. Ochkas, D.Z. Yurchenko, and V.B. Vinokurov: Densification kinetics of boron carbide in hot pressing. *Powder Metall. Met. Ceram.* **26**, 881 (1987).
36. Y. Zeng, J.W. Feng, Y.F. Zhang, and C.X. Ding: Relationship between properties and microstructure of plasma sprayed boron carbide coating. *J. Inorg. Mater.* **15**, 137 (2000).
37. L.S. Wang: The thermal conductivity and thermal expensing coefficient for hot-pressed boron carbide. *J. Cent. South Univ. Technol.* **34**, 111 (2003).
38. F. Deng: *Preparation of Submicron Boron Carbide by Mechanical Alloying* (Dalian University of technology, China, 2005).
39. M. Salvador, J.M. Perlado, A. Mattoni, F. Bernardini, and L. Colombo: Defect energetics of β-SiC using a new tight-binding molecular dynamics model. *J. Nucl. Mater.* **s329–333**, 1219 (2004).
40. E. Rauls: *Annealing Mechanisms of Point Defects in Silicon Carbide*. Ph.D. thesis (English), Theoretical Physics, Department of Physics, Faculty of Science, University of Paderborn, Germany, 2003.
41. E.V. Aleksandrova, A.M. Ilyina, E.G. Grigoryev, and E.A. Olevsky: Contribution of electric current into densification kinetics during spark plasma sintering of conductive powder. *J. Am. Ceram. Soc.* **98**, 3509 (2015).
42. D.M. Zhang: *Study on Mechanism of Pulse Electric Current Sintering of Ceramic Materials* (Wuhan University of Technology, Wuhan, 2002); pp. 11–35.
43. Z. Shen, M. Johnsson, Z. Zhao, and M. Nygren: Spark plasma Sintering of alumina. *J. Am. Ceram. Soc.* **85**, 1921 (2002).

https://doi.org/10.1557/jmr.2017.205 Published online by Cambridge University Press